



# MISR empirical stray light corrections in high-contrast scenes

J. A. Limbacher<sup>1,2</sup> and R. A. Kahn<sup>1</sup>

<sup>1</sup>Earth Science Division, NASA Goddard Space Flight Center, Greenbelt MD 20771, USA

<sup>2</sup>Science Systems and Applications Inc., Lanham MD 20706, USA

Correspondence to: R. A. Kahn (ralph.kahn@nasa.gov)

Received: 23 February 201 – Published in Atmos. Meas. Tech. Discuss.: 09 March 2015

Revised: 12 June 2015 – Accepted: 01 July 2015 – Published: 22 July 2015

**Abstract.** We diagnose the potential causes for the Multi-angle Imaging SpectroRadiometer's (MISR) persistent high aerosol optical depth (AOD) bias at low AOD with the aid of coincident MODerate-resolution Imaging Spectroradiometer (MODIS) imagery from NASA's Terra satellite. Stray light in the MISR instrument is responsible for a large portion of the high AOD bias in high-contrast scenes, such as broken-cloud scenes that are quite common over ocean. Discrepancies among MODIS and MISR nadir-viewing blue, green, red, and near-infrared images are used to optimize seven parameters individually for each wavelength, along with a background reflectance modulation term that is modeled separately, to represent the observed features. Independent surface-based AOD measurements from the AErosol RObotic NETwork (AERONET) and the Marine Aerosol Network (MAN) are compared with MISR research aerosol retrieval algorithm (RA) AOD retrievals for 1118 coincidences to validate the corrections when applied to the nadir and off-nadir cameras. With these corrections, plus the baseline RA corrections and enhanced cloud screening applied, the median AOD bias for all data in the mid-visible (green, 558 nm) band decreases from 0.006 (0.020 for the MISR standard algorithm (SA)) to 0.000, and the RMSE decreases by 5% (27% compared to the SA). For  $AOD_{558\text{ nm}} < 0.10$ , which includes about half the validation data, 68th percentile absolute  $AOD_{558\text{ nm}}$  errors for the RA have dropped from 0.022 (0.034 for the SA) to  $< 0.02$  ( $\sim 0.018$ ).

## 1 Introduction

The research aerosol retrieval algorithm (RA) for the NASA Earth Observing System's Multi-angle Imaging SpectroRadiometer (MISR) is used to analyze regional wildfire smoke,

desert dust, urban pollution, volcanic ash, and other individual events and to test algorithm modifications that might ultimately be applied to the MISR standard aerosol retrieval algorithm (SA) that generates the operational product for the entire MISR data set (e.g., Kahn et al., 2001; Kahn and Limbacher, 2012; Limbacher and Kahn, 2014). The RA relies on the MISR standard Level 1B2 (L1B2) product for radiometrically and geometrically calibrated spectral reflectance data as input for the aerosol retrievals. The spectral aerosol optical depth (AOD), retrieved over water using multi-angle data in the MISR red and near-infrared (NIR) bands, is sensitive to both the absolute reflectance and its spectral dependence, and retrieved aerosol type is even more sensitive to these values (Kahn and Gaitley, 2015). Although considerable effort has produced a MISR Level 1 product with about 3 % absolute radiometric accuracy, and generally even better band-to-band and camera-to-camera relative calibration (Bruegge et al., 2004, 2007; Diner et al., 2004; Kahn et al., 2005; Lyapustin et al., 2007; Lallart et al., 2008), there remain some artifacts in the radiometry that have not been characterized quantitatively (e.g., Bruegge et al., 2004). These can affect both the AOD (including a generally high mid-visible AOD bias of  $\sim 0.02$  for low-AOD cases over dark water) and especially the aerosol type results (e.g., Kahn et al., 2010; Limbacher and Kahn, 2014).

In Limbacher and Kahn (2014), we showed that a small positive bias remained in the RA at low AOD over ocean ( $\sim 0.01$  for the green at  $AOD < 0.10$ ), even with all the adjustments that were implemented in that study. In the current paper, we identify reflections within the instrument (primary and secondary ghosting convolved with background reflectance modulation and blurring) as contributing to, and possibly accounting fully for, the observed bias. We use comparisons with (1) coincident observations by the MODerate-

resolution Imaging Spectroradiometer (MODIS) that flies with MISR aboard the NASA Earth Observing System's Terra satellite to develop empirical corrections to artifacts observed in the MISR/MODIS reflectance ratios in high-contrast scenes. Validation of the stray light corrections is performed using the MISR RA constrained by coincident measurements from (2) AErosol RObotic NETwork (AERONET) surface-based sun and sky scanning photometers (Holben et al., 1998) and (3) the associated Marine Aerosol Network (MAN) sun photometers (Smirnov et al., 2009).

## 2 Validation data sets and validation methodology

MODIS imagery allows for direct radiometric comparison with observations from the MISR nadir-viewing camera only. Results for the full range of MISR cameras are validated to the extent possible by comparing the AOD derived from the MISR RA, using corrected radiometry, with coincident surface-based sun photometer values.

### 2.1 The MODIS data set

MODIS radiometric calibration is based on a combination of on-board solar diffuser, direct space and lunar, and relatively unchanging desert-site observations, all modifying the pre-launch laboratory calibration (Xiong and Barnes, 2006). The most recent systematic refinement of MODIS calibration was performed by Sun et al. (2012), which they determine brings all the MODIS Terra reflective solar spectral bands within about 2 % accuracy at nadir. Lyapustin et al. (2014) used advanced vicarious calibration to identify further adjustments that amount to removing a trend of a few tenths of percent in the MODIS Terra calibration; this stabilizes the derived reflectance time series for desert validation sites and brings MODIS Terra radiometry into better agreement with that of its sister MODIS instrument that flies on the Aqua satellite.

To obtain the best available radiometric accuracy, we apply the Lyapustin et al. (2014) adjustments to the MODIS Collection 6 Level 1B 1 km reflectance data when making comparisons with MISR (except for bands 13 and 14, because corrections are unavailable for these channels). The MISR spectral bands are centered at 446 (blue), 558 (green), 672 (red), and 866 nm (NIR). MODIS bands closest to the MISR ones are bands 9 (443 nm, blue), 4 (555 nm, green), an average of bands 13 and 14 (effective 672 nm, red), and 2 (856 nm, NIR). The MISR–MODIS comparisons in this study are performed for the closest spectral band (or bands) and where the contrasts are greatest, i.e., over dark water scenes with well-defined, bright ice or cloud patches. Saturation is not a problem for bands 9, 13, and 14 when optimizing the ghosting parameters because we only use the MISR/MODIS ratios over dark portions of the scenes, where the ghosting signal is highest. MISR observations are coin-

incident with MODIS Terra (hereafter just MODIS) and capture approximately  $\pm 190$  km in the center of the 2300 km MODIS swath, so MODIS swath-edge and scan-angle issues are minimal or non-existent for the analysis performed here.

### 2.2 The MAN/AERONET data set

Surface-based sun photometers provide ground truth for satellite AOD retrieval validation (e.g., Kahn et al., 2010; Levy et al., 2013). The AERONET CIMEL instruments are calibrated periodically against standard instruments and provide AOD measurement accuracy of approximately  $\pm 0.01$  at  $\sim 550$  nm wavelength (Eck et al., 1999). The hand-held MicroTops instruments used for MAN shipboard observations offer AOD accuracy of approximately  $\pm 0.02$  (Smirnov et al., 2009). Ångström exponents (ANGs) used for validation were calculated from the sun photometer AOD values by first interpolating to the four MISR effective wavelengths using a second-order polynomial fit in log space and then finding the slope of the least-squares line fit to the interpolated AOD values also in log space, as we have done in previous studies. We obtained 178 near-coincident MAN and 940 AERONET over-water or island observations to compare with AOD retrieved with the RA, using the recalibrated MISR reflectances. Further description of the globally distributed, AERONET/MAN coincident data set used here is given in Limbacher and Kahn (2014).

### 2.3 The MISR research algorithm

Details of the MISR RA as applied in this paper can be found in Limbacher and Kahn (2014). Briefly, over water, the RA compares the MISR-observed equivalent reflectances with simulated top-of-atmosphere (TOA) values for a range of aerosol component and mixture optical models. All (aerosol-mixture/AOD) pairs that meet an adaptive  $\chi^2$  test criterion, which includes absolute and relative components, are considered adequate matches to the observations. The lower boundary condition in the simulations is represented as a black, Fresnel-reflecting ocean surface with glitter masking and standard wind-speed-related whitecap modeling, plus under-light due to molecular scattering, near-surface dissolved organic matter, and chlorophyll *a*. Where available, wind and ocean-color constraints were obtained from the daily Cross-Calibrated Multi-Platform (CCMP) (Atlas et al., 2011) and GlobColour (Barrot et al., 2010) products, respectively, and from climatology elsewhere. All the physical and empirical RA upgrades described in Limbacher and Kahn (2014) were applied where the RA is used, including the empirical radiometric adjustment to the red and NIR bands; nominal cloud screening from the MISR SA is applied, but where noted below we perform additional cloud screening based on the fraction not clear (FNC), as described in Limbacher and Kahn (2014). For the purposes of the current paper, we refer to the RA, including all these upgrades except the FNC ad-

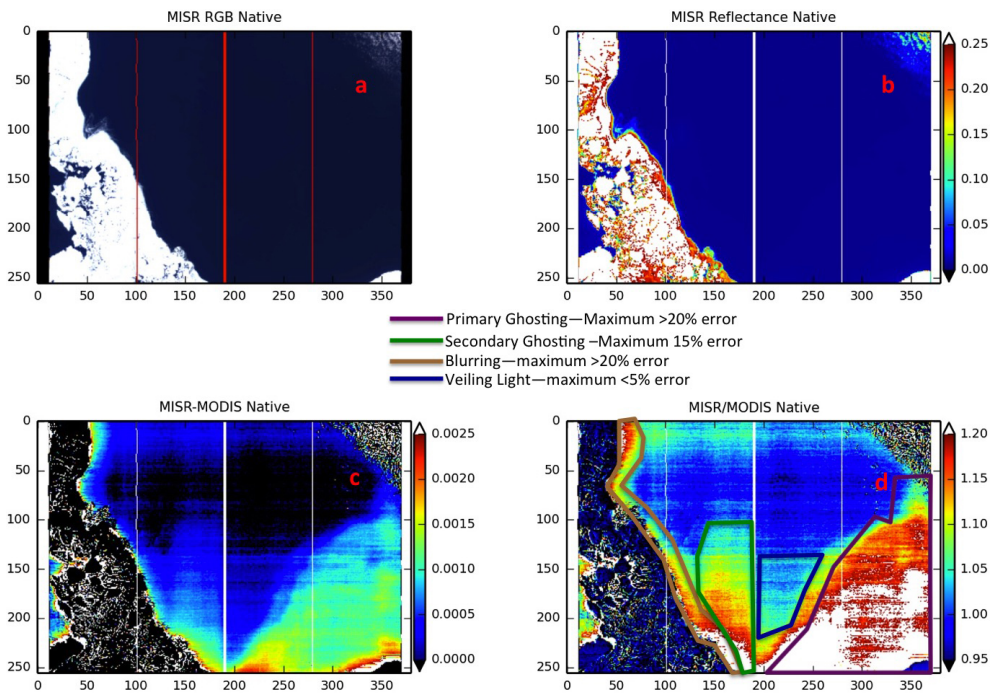


**Figure 1.** (a) MISR nadir-view (AN) RGB reflectance context image of an ice-and-dark-water scene. (b) MISR AN NIR reflectance for the scene. (Reflectance scale to the right of the image.) (c) (MISR (AN NIR) – MODIS (NIR)) reflectance differences. (Difference scale to the right of the image.) (d) (MISR (AN NIR)/MODIS (NIR)) ratios for the scene. The four contours in this panel outline approximately the areas where optical anomalies occur (color key in the middle of the figure). The image presented corresponds to MISR orbit 58 388, blocks 152–153. The vertical lines stretching down the images represent the 25th, 50th, and 75th percent of the image that contains valid data. Native refers to the fact that the MISR data have been rotated to their native (L1B1) format. The x axes for (a)–(d) represent a modified MISR sample number (some of the fill values on the edges of the swath were removed), and the y axes in (a)–(d) represent MISR line number.

justment, as the “baseline” RA. The initial MISR–MODIS reflectance comparisons are performed with the standard MISR L1B2 data, with the appropriate out-of-band corrections (Chrien et al., 2001) applied.

For global-mode observations, MISR data are acquired at 275 m or 1.1 km pixel resolution, depending on the channel. For this study, all MISR data are resampled to 1.1 km from 275 m (where appropriate), which means that there are  $\sim 360$  pixels across the entire MISR swath for the nadir-viewing (AN) camera. TOA reflectances for the RA are obtained from these resampled reflectances, as are the reflectances used for comparison to MODIS. The coefficients derived in this paper are valid for the 1.1 km resolution data; some values would need to be recalculated for applications using data at 275 m resolution.

#### 2.4 MISR calibration approach

We studied the ratio of MISR to MODIS reflectances across the MISR nadir-camera swath as a means of identifying possible calibration anomalies. We rely on MODIS as the standard in this application, as MODIS is a cross-track scanning instrument whereas MISR is a push-broom imager, having fixed viewing optics that observes around the center of the

MODIS swath. (As such, “ghosting” would show up along the spacecraft ground track for MODIS, and “latency” would operate across track. It is the opposite for MISR, making it possible to separate these issues. See below.) Ocean scenes partly filled with ice or very distinct clouds were selected (e.g., Figs. 1a, 2a, and 3a) to provide sharp brightness contrast features that can highlight artificial reflections and other imaging issues. We considered three possible sources of radiometric artifacts in the MISR data:

1. Stray light, which includes reflections from the camera optics into the detector as well as a mischaracterized point spread function. For internal reflections, this would produce a pattern of reduced contrast in high-contrast scenes: brightening over darker regions and darkening over bright regions. The effect should be absent over uniformly bright or dark scenes and would include veiling light, which amounts to uniformly spread radiance over the detector, and “ghosting,” which accounts for more structured reflectance features at the detector. A mischaracterized point spread function could theoretically lead to either too much or too little contrast in high-contrast regions, especially along edges where the reflectance gradient is high.

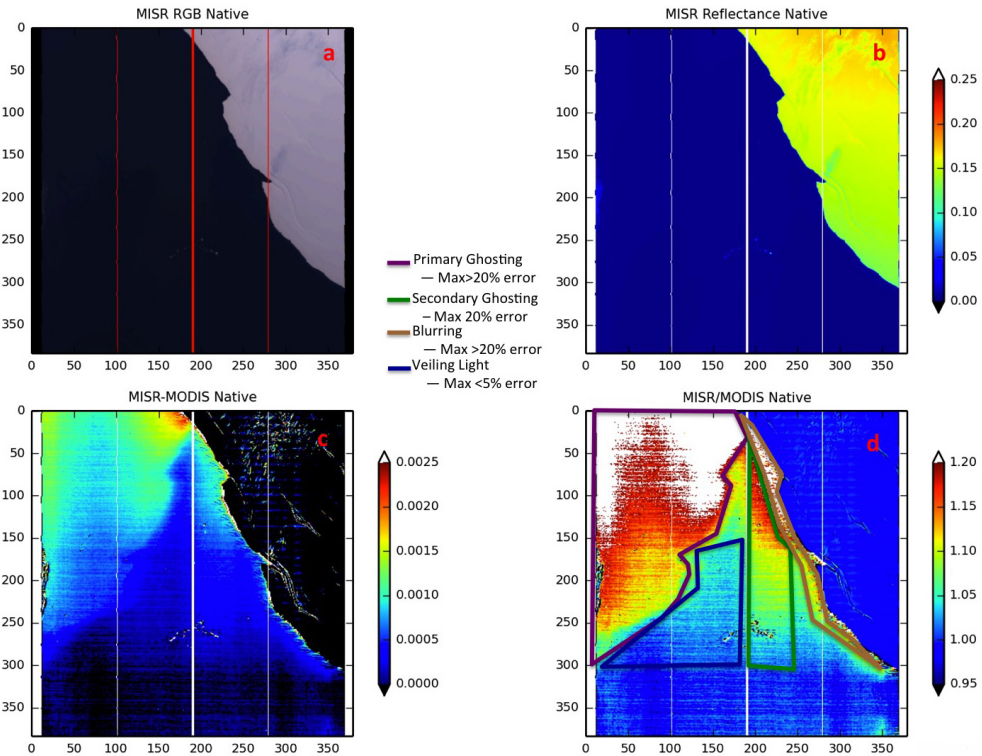


**Figure 2.** Same as Fig. 1 but for MISR orbit 10 793, blocks 169–171.

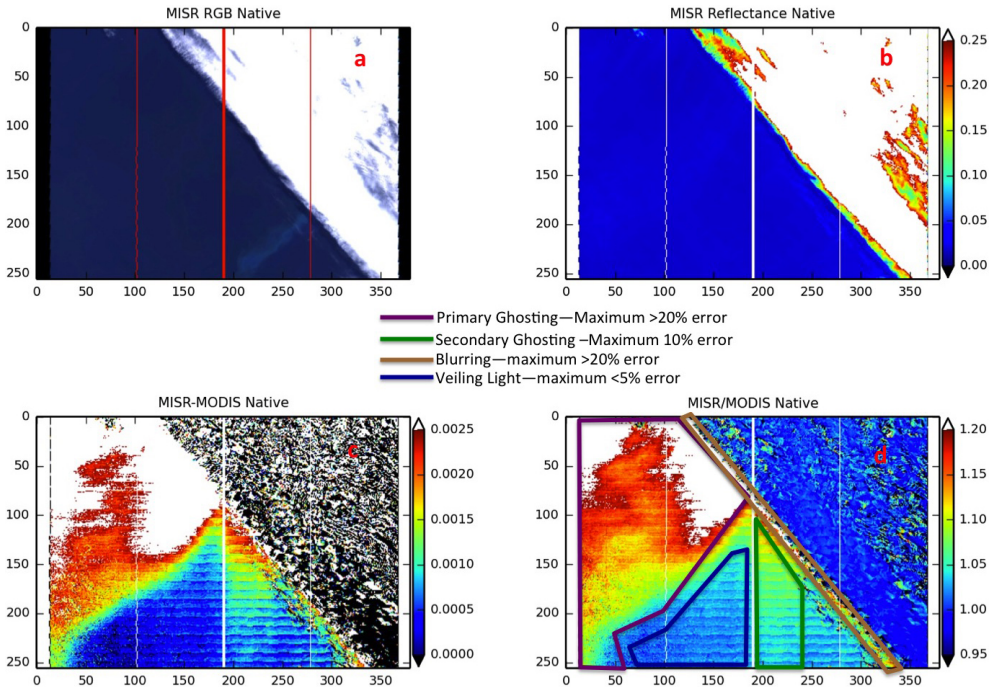


**Figure 3.** Same as Fig. 1 but for MISR orbit 21 701, blocks 132–133.

2. Latency, which amounts to pixels retaining signal from previous fields of view. For a given pixel, this would produce brightening as the detector moves from a bright

to a dark target and would be especially apparent when crossing a sharp edge, e.g., snow-covered land or sea-ice to dark ocean. The converse would occur moving

from dark to bright targets, though the signal might be less apparent.

3. Radiometric calibration artifacts, which could include flat-fielding errors that appear as features in the imagery of an otherwise uniform scene. These errors could be introduced due to uncertainty in modeling the Spectralon panels used for the on-board calibration of MISR or because of uncompensated non-uniform responses by different pixels at the detector. For the nadir camera, comparison with MODIS Terra over uniform scenes could test for such artifacts.

We began by converting the MISR Level 1B2 radiance data to equivalent reflectance, applying the out-of-band corrections to the data (Chrien et al., 2001), and resampling to 1.1 km from 275 m for all channels in the nadir camera and red bands of the off-nadir cameras. Stray light and latency would affect the original MISR line-array detector pixels, whose output is recorded in the MISR Level 1B1 (L1B1) product. The MISR Level 1B2 pixel-level data are resampled from the original Level 1B1 data, taking account of geometric and radiometric calibration considerations (Bruegge et al., 1999; Jovanovic et al., 1999, 2002), and are used in the aerosol retrievals. As the L1B1 data are only archived for the most recent 90 days of acquisition, we had to work with L1B2 data to obtain the required scene types for subsequent analysis. To relate the L1B2 to the L1B1 data, we first approximately undid the L1B2 geometric resampling for cases where L1B1 data were also available by rotating the index matrices corresponding to the region of interest. The equations of rotation for a 2-D array are

$$\begin{aligned}x' &= x \cos(\theta) - y \sin(\theta) \\y' &= x \sin(\theta) + y \cos(\theta).\end{aligned}\quad (1)$$

Here,  $x$  and  $y$  correspond to the  $x$  (along-track) and  $y$  (across-track) location index arrays.  $\theta$  represents the rotation angle, and, because we use a left-hand coordinate system, a positive  $\theta$  corresponds to clockwise rotation. The rotation is performed about the center pixel on each line separately and varies based on latitude, camera, and sample. We adopted empirical values for the camera-by-camera angles of rotation ( $\theta$ ) that are determined with an optimization algorithm that matches the corresponding rotated L1B2 data to available L1B1 data. This algorithm first shrinks or expands the valid L1B2 data until they fit the L1B1 data, then proceeds to rotate the data by an angle which varies with latitude and by a fixed angle for each camera (for each of the right half and left half of the scenes), a process that corresponds to unwrapping the data from the ellipsoid (Earth) to which the L1B2 data are projected. The optimization routine maximizes the correlation between the L1B1 data and the new rotated data set derived from the corresponding L1B2 data, for a validation set of L1B1 data to which we had access. This process yields both the latitudinally dependent angle correlating to

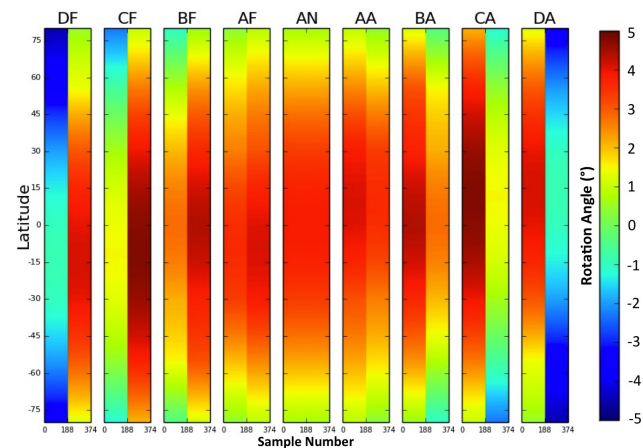


**Figure 4.** These nine plots represent the empirically derived rotation angles used to bring MISR L1B2 data into agreement with MISR L1B1 data, as a function of latitude and MISR sample number along the focal plane line array, for each camera. The camera designations used in this figure are D = 70.5°, C = 60°, B = 45.6°, A = 26.1°; F is the forward-viewing camera; A is the aft-viewing camera; AN is the nadir-viewing camera. Because these angles were calculated empirically using an optimization routine, the rotation angles are approximate.

the Earth's rotation and the fixed angle required to unwrap the image from the ellipsoid. Figure 4 shows the optimized rotation angle as a function of latitude and sample along the focal plane line array for each camera. Note the difference in the rotation angle between left and right halves of the swaths for the off-nadir cameras, representing the components of the rotations about the middle of the detector arrays. Ideally, the stray light corrections should be implemented in the MISR Level 1A processing, to avoid these approximations and other limitations imposed when the data are processed to Level 1B2, such as the L1B2 imagery being trimmed near the poles.

After rotation, the coincident 1 km MODIS Terra reflectance data were re-gridded using a nearest-neighbor approach to match the rotated 1.1 km MISR reflectance data, so reflectance ratios and differences could be plotted (e.g., panels c and d of Figs. 1, 2, and 3) and analyzed. We determined radiometric corrections empirically by iteratively testing and adjusting the coefficients of functions representing the observed anomaly patterns in the MISR reflectance images of high-contrast scenes using an optimization scheme, as described in the next section. A flow chart of the entire calibration-adjustment-determination process is given in Fig. 5.

### 3 MISR calibration refinement

Because the spectral response functions of MISR and MODIS are different, the normalization required to apply

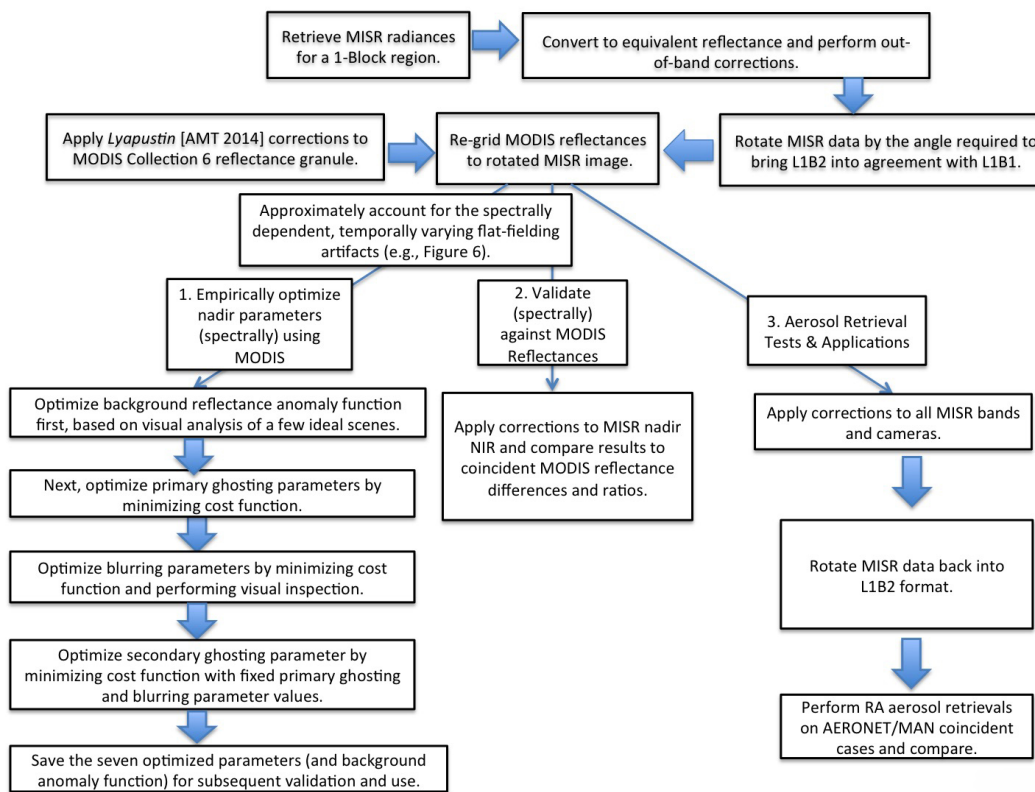


**Figure 5.** Flow chart summarizing the steps involved in the MISR stray light corrections.

comparative image analysis on a given scene can depend on viewing geometry, solar geometry, and aerosol loading and does not necessarily represent degradation in either instrument. For the remainder of Sect. 3, we normalize the MISR reflectances for each scene empirically, so the dark parts of the normalized scenes, away from the influence of any contrast features, retain a MISR/MODIS ratio of  $\sim 1.0$  from the beginning to the end of the mission. The normalization required for the cases studied falls in the range of  $0.98 \pm 0.02$  for the blue,  $1.03 \pm 0.02$  for the green,  $0.985 \pm 0.005$  for the red, and  $1.025 \pm 0.025$  for the NIR, depending on the scene.

We identified specific patterns in the normalized MISR/MODIS ratio images where MISR systematically overestimates or underestimates the TOA reflectance, as compared to MODIS. Examining pixel reflectance data where the MISR push-broom line arrays moved first over a bright, snow-covered surface and then across a sharp contrast transition to dark water, we found no evidence of latency effects.

### 3.1 Approximate flat-fielding correction

However, we did find evidence suggesting that the MISR L1B2 imagery has embedded flat-fielding artifacts. We present an example of such artifacts in Fig. 6, which shows RGB and green band reflectance data over a very uniform

Greenland scene, orbit 13 329, block 27. The MISR and MODIS reflectance data used to create these plots are first normalized such that their mean value is 1.0. Looking at Fig. 6b, which is MISR data alone, it is fairly apparent where the flat-field artifacts are present, as the data appear blurred across multiple lines. Figure 6e gives a more quantitative indication as to the magnitude of these errors, which reach their maxima at  $\pm 1\%$ .

Although we only present evidence for this flat-fielding error for the green band in Fig. 6, the error is found in all four MISR channels at nadir. The error patterns for the blue and green bands are very similar yet different from those for the red and NIR, which are also similar to each other. We suspect that uncorrected variation in the Spectralon panel reflectances is the source of these anomalies, because the blue and green AN channels are calibrated against one MISR on-board Spectralon panel whereas the red and NIR AN channels are calibrated against the other panel. The errors tend to be no more than about  $\pm 1\%$  for the image shown in Fig. 6; however, such errors could significantly impact particle type results if the blue or green channels are included in the retrievals. Also, these errors are significantly greater than the 0.5 % expected pixel-to-pixel error.

For the remainder of Sect. 3, we automatically correct the MISR reflectances for the flat-fielding artifacts by taking two uniform scenes, one near mission start and one in 2014,

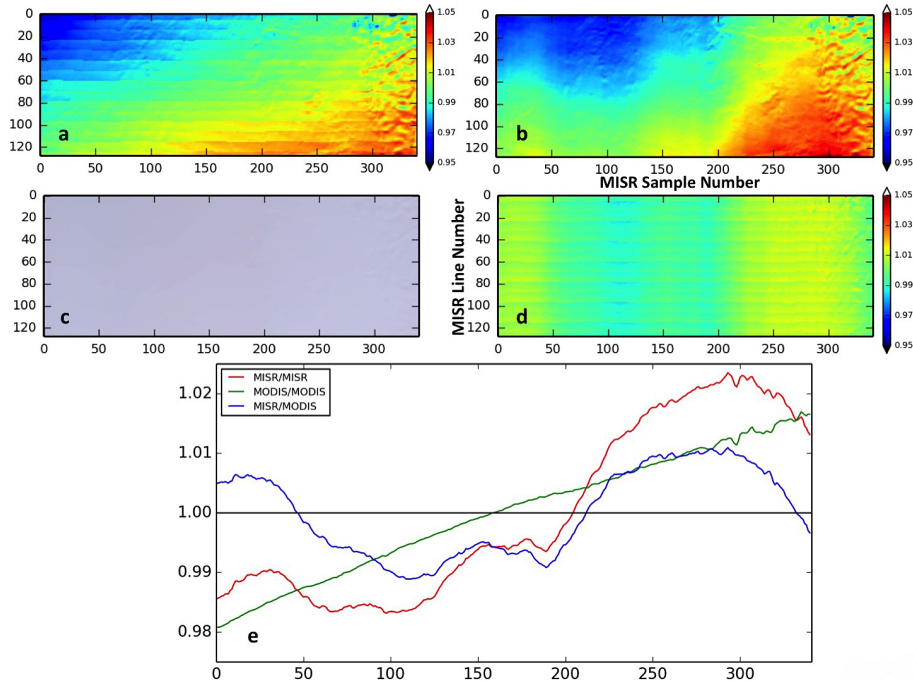


**Figure 6.** Approximate flat-fielding using a uniform scene. The data in this image are from Terra orbit 13 329, block 27. The  $x$  axis in each image represents a modified MISR sample number (the fill values on the edges of the swath were removed), whereas the  $y$  axes in (a)–(d) represent MISR line numbers. (a) MODIS band 4 normalized reflectance for the scene. (b) MISR AN green band normalized reflectance. (c) MISR RGB image for the scene, which was taken over Greenland. (d) MISR (normalized)/MODIS (normalized) reflectances for this scene. Notice that the vertical stripes present in the data appear unrelated to the MODIS horizontal striping issue. (e) Line-averaged MISR/MISR across sample mean (red plot), line-averaged MODIS/MODIS across sample mean (green plot), and line-averaged MISR/MODIS (blue plot). Notice that the MODIS reflectances decrease linearly across the scene, whereas the MISR reflectances have three distinct peaks. The MISR/MODIS ratios can be thought of as the MISR flat-fielding error for this scene, and the errors maximize at roughly  $\pm 1\%$ .

fitting curves to the MODIS/MISR ratios for each spectral band, and interpolating linearly over time. We then multiply this temporally interpolated curve by the MISR reflectances to approximately remove the flat-fielding artifacts for all steps discussed subsequently in this paper. We show the impact of the flat-fielding corrections by plotting the MISR-over-MODIS ratios (blue band only) both without (Fig. 8b) and with (Fig. 8c) these flat-fielding artifacts corrected. A more in-depth treatment of the flat-fielding error is beyond the scope of the current paper, but we and other MISR team members are working to further quantify and correct these artifacts (Limbacher and Kahn, 2015; C. Bruegge, personal communication, 2015).

### 3.2 Stray light correction modeling

We also identified three separate phenomena affecting the light impinging on the MISR focal plane in high-contrast scenes that could be described as forms of stray light: primary ghosting, secondary ghosting, and blurring. In addition, a non-linear background variation in the MISR/MODIS reflectance ratio appears to modulate the primary ghosting anomaly. (This background variation is distinct from the flat-

fielding discussed in Sect. 3.1 above, as it applies only to ghosting that occurs in non-uniform scenes.) The stray light effects are generally small, probably amounting to a few percent or less in many scenes globally, especially over land. However, the effects can be much larger in high-contrast scenes; even in less extreme situations, they can have a substantial impact on aerosol retrievals, particularly at low AOD over dark water, as we demonstrate below. In this section, we define empirical models for the three effects and the associated background modulation, as these contributions are large enough to quantify with our image-analysis approach.

The first effect is a mirroring of the image about a line drawn down the center of the scene (Figs. 1d, 2d, 3d, purple outlines). The following equation approximates the error due to this mirroring, which we identify subsequently as “primary ghosting”:

$$\text{Ghost}_1 = b_i \cdot C_1 \left( \rho_i - \frac{\sum_{n=-r_1}^{r_1} (\rho_{i+n}^{\text{mirror}}) \{|n|+1\}^{-p_1}}{\sum_{n=-r_1}^{r_1} \{|n|+1\}^{-p_1}} \right). \quad (2)$$

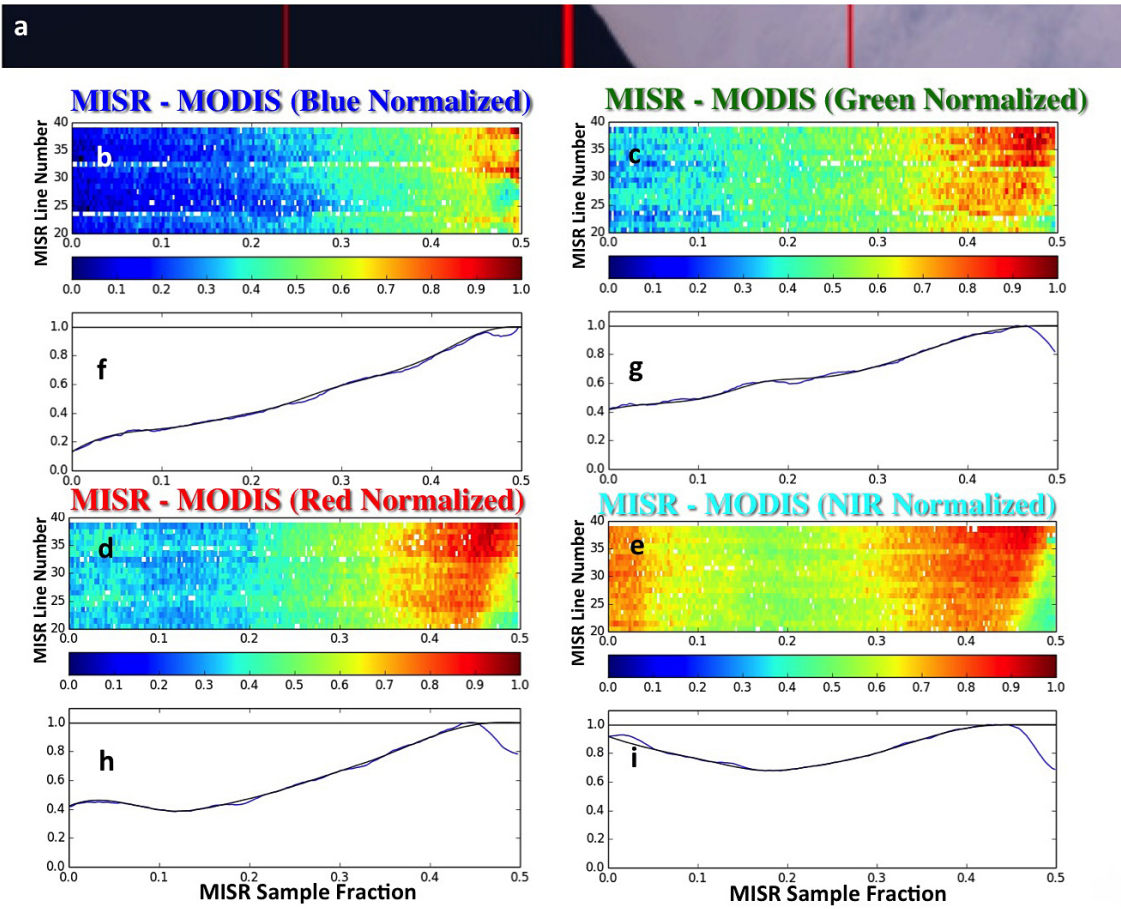


**Figure 7.** Background modulation of the primary ghost. The  $x$  axes in (b)–(i) correspond to the fractional positions within the scenes (in this case the left half of scene a). (a) MISR RGB image for orbit 10 793, block 169, lines 20–40. The vertical red lines represent the 25th, 50th, and 75th percentiles of the scene. (b–e) MISR–MODIS reflectance difference image corresponding to the left half of the scene in (a). The  $y$  axis represents the line number (MISR lines 20–40). The MISR–MODIS reflectance differences are scaled so the maximum value for the left half of the scene is unity, after outliers ( $\text{median} \pm 2$  standard deviations for a constant sample) are removed. If the primary ghost were uniform, we would expect values close to 1 for nearly the entire left half of the scene. (f–i) The blue lines on these plots represent the line-averaged values of the normalized reflectance differences (b–e) normalized such that the maximum line-averaged value is unity, whereas the black lines represent analytical functions adjusted by hand to approximately fit these data. Notice the large differences between channels. Because these functions only cover half the swaths, we assume that they are mirrored to the other side of the swath as well. To correctly model the primary ghosting term, we multiply this function by the ghosting term.

$C_1$  represents the mirror amplitude,  $\rho_i$  is the MISR-reported reflectance at pixel  $i$  in the camera line array,  $\rho_i^{\text{mirror}}$  is the MISR-reported reflectance at pixel  $i_{\text{mirror}}$  in the camera line array, and  $r_1$  gives the range of pixels over which the reflectance from pixel  $\rho_i$  makes mirroring contributions. The  $r_1$  parameter is set to the entire  $x$  axis for the scene (e.g., if there are 360 1.1 km pixels in the scene across track,  $r_1$  is set to 360). This allows the primary ghosting term to take into account some blurring of the mirror image. The  $p_1$  parameter provides distance weighting to account for decreasing contributions away from the mirroring peak. If the primary ghost produced a perfect mirror image of the bright pixels,  $p_1$  would approach infinity and the contribution from any pixel except the mirror pixel would approach 0. Be-

cause  $\rho_i - \rho_i^{\text{mirror}}$  represents the contrast between the mirror pixel and the corresponding image pixel, the mirroring coefficient is multiplied by this difference on the right-hand side of Eq. (2) to produce an approximate contrast correction. The weighting includes  $|n|$  so the contributions are symmetric about  $\rho_i$ , and 1 is added to avoid arbitrarily setting the mirror pixel reflectance to 0 at  $n = 0$ .

The background non-linear reflectance function, that appears to modulate the primary ghost relative to MODIS, is represented by  $b_i$ . It was computed by identifying a specific scene where about half the image appears homogeneous and dark and the other half uniform and bright, so a nearly constant mirroring correction should be required if there were no background modulation. Once such a scene was identified

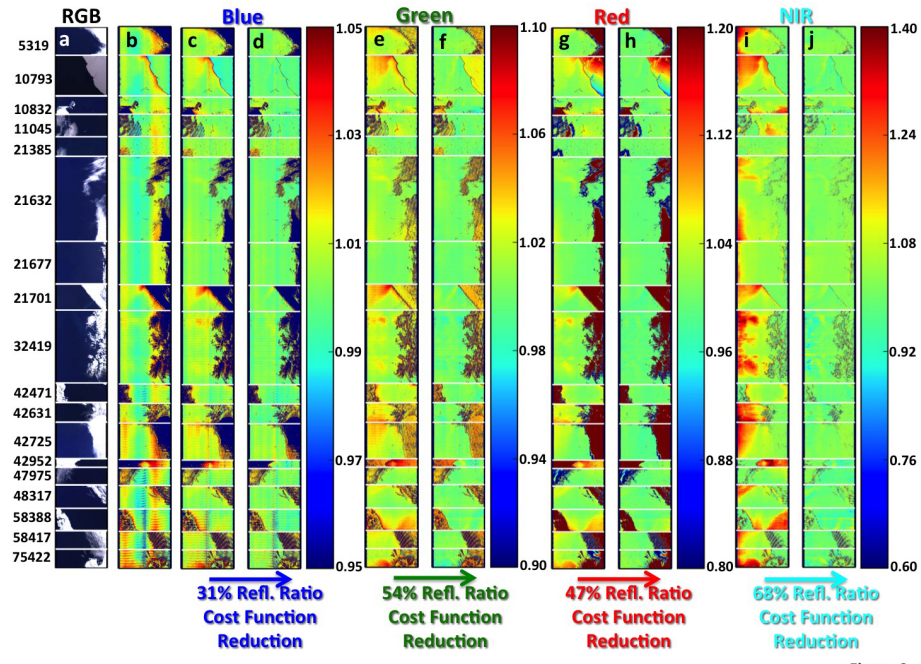


Figure 8

**Figure 8.** (a) MISR nadir contrast-enhanced RGB images for 18 different scenes, concatenated, and separated by thin white horizontal lines. Numbers to the left indicate Terra orbit. (b) MISR/MODIS reflectance ratios for the blue with no flat-fielding corrections. Notice the flat-fielding artifacts running vertically up and down the image at very specific locations. (c, e, g, i) MISR/MODIS reflectance ratios for the blue, green, red, and NIR, respectively, before ghosting corrections are applied to the data. MISR data have been corrected for flat-fielding artifacts. (d, f, h, j) MISR/MODIS reflectance ratios after ghosting corrections are applied to the data. The scale is to the right of each set of data.

(Fig. 7), we scaled the MISR–MODIS reflectance differences so the maximum value is unity and fit a function to the corresponding normalized differences by eye (Fig. 7f–i). To get the fit function for the other half of the image, we assume that the function is symmetrical about the center of the image.

Figure 8 presents 18 high-contrast images spanning the MISR mission, shown here both before and after the primary ghost, and its background modulation, and the other ghosting corrections are applied. It illustrates, among other things, how the flat-fielding correction reduces the vertical striping that is especially apparent in Fig. 8b (and corrected in Fig. 8c). The corrected images also include the background reflectance modulation function (applied to the primary ghosting term), which acts to improve the primary ghosting correction (e.g., see the area within the purple outline in Fig. 2d to get an idea of the non-uniformity of the primary ghosting correction).

The second correction approximates the secondary ghosting effect that appears to impact scene halves, supplementing the primary ghost with a smaller, more uniform reflected light contribution (Figs. 1d, 2d, 3d, green outlines). The following equation represents this error in a simplified manner:

$$\text{Ghost}_2 = C_2 \left( \rho_i^{\text{half}} - \langle \rho^{\text{half}} \rangle \right). \quad (3)$$

Note that Eq. (2) collapses to this form (without the background modulation term) when the power parameter is set to 0.0 and the distance parameter ( $r$ ) is set to half of the  $x$  axis ( $\sim 180$  1.1 km pixels at nadir).  $C_2$  is the secondary ghosting amplitude over the half of the scene in question,  $\langle \rho^{\text{half}} \rangle$  represents the average scene reflectance over half the image, and  $\rho_i^{\text{half}}$  is the MISR-reported reflectance at pixel  $i$  in the half of the camera line array being evaluated. As such, there are in principle two secondary ghosting terms to compute separately for each image, one for each half of the scene. In practice, we determine the ghosting parameters in Eqs. (2) and (3) simultaneously over all 18 scenes shown in Fig. 8, some with the bright feature in the left half of the image and some with the bright feature on the right, and assume the corrections are symmetrical about the swath center. This assumption is consistent with the level of detail that can be extracted with the image-analysis approach from the data used in the current study.

We found it necessary to add a third effect that amounts to a blurring of the image, observed most readily along edges of high contrast, similar to a modified point spread function (Figs. 1d, 2d, 3d, brown outlines). The following equation

approximates the error due to image blurring:

$$\text{Blur} = C_3 \left( \rho_i - \frac{\sum_{n=-r_3}^{r_3} (\rho_{i+n}) \{|n| + 1\}^{-p_3}}{\sum_{n=-r_3}^{r_3} \{|n| + 1\}^{-p_3}} \right), \quad (4)$$

where  $C_3$  is the blur amplitude and, again,  $r_3$  and  $p_3$  define the range of pixels impacted and the distance weighting, respectively. The blur adjustment is applied over the entire image, but it has by far the biggest effect on scene elements having very high contrast, such as cloud and ice edges over dark water. We refer to the aggregate of the three effects represented by Eqs. (2), (3), and (4) as our empirical “ghosting” correction.

An additional effect, uniform veiling light, typically represents a very small fraction of the total anomaly signal (Figs. 1d, 2d, and 3d, blue outlines), too small to quantify numerically with our empirical image-analysis approach. Although we attempted to model veiling light as an explicit term in the empirical optimization routine, it gave us values of essentially 0 for the resulting veiling-light coefficient (analogous to  $C_1$  in the Eq. 2 above). However, this phenomenon is still corrected to some degree by the primary and secondary ghosting terms.

### 3.3 MISR stray light correction parameter optimization using MODIS

Eighteen high-contrast, low-AOD MISR and MODIS over-water scenes spanning December 2000 (early in the MISR mission) to February 2014 were used to optimize the “C,” “ $r$ ,” and “ $p$ ” parameters from Eqs. (2), (3), and (4), as shown in Fig. 8a. (The “ $b_i$ ” correction in Eq. (2) is determined separately from the background MISR/MODIS reflectance ratio, as discussed relative to Fig. 7.) The parameter optimization is done only for the nadir camera because we only have MODIS nadir-viewing data.

The method of optimization involves minimizing the following cost function:

$$\text{Cost} = \frac{\sum_{i=0}^n \left| 1.0 - \frac{\text{MISR}_{\text{new}}}{\text{MODIS}} \right|}{n}. \quad (5)$$

Here,  $\text{MISR}_{\text{new}}$  represents the corrected MISR pixel reflectance, MODIS is the nearest MODIS pixel reflectance, and  $n$  represents the number of data points used for the parameter optimization. We apply this cost function because it is not very sensitive to outliers (no squared quantities) that could be present (e.g., due to data collocation errors).

Because we perform the optimization using several hundred thousand data points, it would be too computationally time consuming to treat all seven parameters simultaneously. First we make the assumption that we can average the power and distance terms by wavelength ( $p_1$  and  $r_1$  for example) to

get one effective value of each. We then set  $r_1$  equal to the entire scene  $x$  axis as described in Sect. 3.2 and optimize the primary ghosting parameters  $C_1$  and  $p_1$  in Eq. (2) for each band separately. This is done using only the portion of the scene where the primary ghosting clearly occurs (i.e., where bright regions are reflected across the image centerline, such as the purple outlines in Figs. 1d, 2d, and 3d). We assume that the correction continues into the other half of the image but with diminishing power (based on the value of  $p_1$ ); this is difficult to test empirically in the brighter portions of the image, but it has the effect of eliminating sharp cutoffs. To avoid the brighter cloud or ice-covered regions, where geolocation error can create large apparent reflectance anomalies, we mask any places where the MISR or the MODIS data are greater than some adaptive cutoff, which we take as a wavelength-dependent factor times the fifth percentile value for the aggregated MISR or MODIS reflectance data, respectively. The factors, determined empirically, are 1.3, 1.8, 2.75, and 5 for the blue, green, red, and NIR bands, respectively. These multipliers were chosen such that the same amount of data, to within a couple of percent, are used for the optimization in each wavelength. Information on cost function reduction as well as all of the optimized ghosting coefficients can be found in Table 1.

We then optimize the three parameters relating to blurring simultaneously, using a few select scenes, by minimizing the cost function and then checking the result by visual inspection. It is important to emphasize that simply minimizing the cost function on a particular data set is not sufficient; to derive the correction parameters that will subsequently be applied generally, the data require proper masking that can only be achieved by iterative trial and error. Once the blurring coefficients were optimized, we tested them using the full 18 scenes of Fig. 8 to ensure the results are robust. We then optimize the secondary ghosting term (Eq. 3) using the darker regions in the bright half of the scene using the same masking technique that was used for the primary ghost optimization. All of the coefficients relating to the ghosting corrections are given in Table 1, along with the cost function values before and after corrections are applied. It is important to note that we have to include the primary ghosting corrections when we optimize the secondary ghosting and blurring terms, because the primary ghosting correction blends into the other half of the image. Note that segmenting the image is required only when deriving the ghosting correction parameters; once determined, the corrections are applied over entire images. Taken together, all seven configurable parameters (plus the background reflectance anomaly function) reduce the cost function by 31, 54, 47, and 68 % for the  $\sim 1$  million data points at each wavelength that are not masked over the scenes. We validate these results in the next section.

**Table 1.** Ghosting parameters and error statistics for 18 scenes used in optimization.

Primary ghost (applied to dark halves of scenes)											
Band	$C_1$	$r_1$	$p_1$	$C_2$	$C_3$	$r_3$	$p_3$	$\text{Cost}_0$	$\text{Cost}_1$	Fr. cost reduction	#
Blue	0.01325	380	0.625					0.0088	0.0057	0.3483	648 489
Green	0.01225	380	0.625					0.0213	0.0081	0.6182	648 732
Red	0.009	380	0.625					0.0265	0.0110	0.5838	648 740
NIR	0.013	380	0.625					0.1160	0.0280	0.7586	648 455
Primary + secondary ghosting and blurring (applied to the bright halves of scenes)											
Band	$C_1$	$r_1$	$p_1$	$C_2$	$C_3$	$r_3$	$p_3$	$\text{Cost}_2$	$\text{Cost}_3$	Fr. cost reduction	#
Blue	0.01325	380	0.625	0.0025	0.025	75	1.35	0.0107	0.0081	0.2463	324 967
Green	0.01225	380	0.625	0.00275	0.025	75	1.35	0.0236	0.0142	0.3984	333 031
Red	0.009	380	0.625	0.001	0.015	75	1.35	0.0282	0.0208	0.2613	332 489
NIR	0.013	380	0.625	0.00275	0.018	75	1.35	0.0762	0.0411	0.4607	331 183
Primary + secondary ghosting and blurring (applied to the full scenes)											
Band	$C_1$	$r_1$	$p_1$	$C_2$	$C_3$	$r_3$	$p_3$	$\text{Cost}_4$	$\text{Cost}_5$	Fr. cost reduction	#
Blue	0.01325	380	0.625	0.0025	0.025	75	1.35	0.0094	0.0065	0.3077	980 697
Green	0.01225	380	0.625	0.00275	0.025	75	1.35	0.0220	0.0102	0.5388	989 020
Red	0.009	380	0.625	0.001	0.015	75	1.35	0.0270	0.0144	0.4680	988 476
NIR	0.013	380	0.625	0.00275	0.018	75	1.35	0.1023	0.0324	0.6836	986 887

Columns 2–8 show the various ghosting parameters as a function of wavelength.  $\text{Cost}_0$  represents the initial cost function before any ghosting corrections are applied, whereas  $\text{Cost}_1$  represents the cost function after the primary ghosting correction is applied, assessed over the dark halves of the scenes. Similarly,  $\text{Cost}_2$  and  $\text{Cost}_3$  are the cost functions before and after all the ghosting correction are applied, respectively, assessed over the bright halves of the scenes.  $\text{Cost}_4$  and  $\text{Cost}_5$  are the cost functions before and after all the ghosting correction are applied, respectively, assessed over the full scenes. The final columns give the numbers of data points used to calculate the cost functions.

## 4 Combined correction and validation using the MISR research algorithm

Unlike MODIS, MISR has multiple view angles, so we require a different way to validate corrections to the eight other MISR cameras. We attempted to use forward model radiative transfer results computed from the MISR/MAN coincidences to compare with the TOA reflectances from MISR (e.g., Kahn et al., 2005). However, the uncertainties in the forward model for each channel separately can be larger than the error due to stray light, which brings into question our ability to validate the seven ghosting coefficients separately for each channel. Instead, we (1) apply the nadir stray light corrections to the MISR TOA reflectances for all 36 channels under the assumption that the effects are dominated by similarities in the optics geometry of the different cameras. (This assumption is the subject of continuing study; Limbacher and Kahn, 2015.) We then (2) run the RA with all the adjustments made in Limbacher and Kahn (2014) on the corrected reflectances both with and without the enhanced cloud screening, and (3) compare the RA-retrieved AODs and Ångström exponents with results from 1118 coincident MAN/AERONET observations for validation and with the corresponding SA retrievals. We modified the calibration adjustments applied to the radiances in Limbacher and Kahn (2014; +0.75 % for the red and -0.75 % for the

NIR). With the ghosting corrections applied, we instead adjust the red TOA radiance by +0.50 % and the NIR by -0.50 %. This was necessary because the ghost images contribute a much larger fraction to the background reflectance in the dark, over-water NIR band compared to the red band. We also modified the acceptance criterion at low AOD from that used in Limbacher and Kahn (2014) as a result of the corrections that are applied to the TOA reflectances. We select all mixtures falling within the minimum  $\chi^2$  value +1.25 at low AOD, rather than the minimum  $\chi^2$  value +0.35, after the corrections are applied. This avoids artificially constraining aerosol type at low AOD; the need occurs because the denominator of the  $\chi^2$  variable, which represents the measurement uncertainty, decreases (often substantially at low AOD) due to the corrections applied here (see Limbacher and Kahn, 2014).

### 4.1 Modifications to uncertainty envelopes and calibration adjustments

Because the fraction of data falling below a given error criterion is highly dependent on retrieved AOD, we modified the “uncertainty envelopes” used to report agreement with validation data from those of previous MISR validation papers. Specifically, we find the size of the envelope so  $\sim 68\%$  of the data falls within it at all AODs. We divided the AOD results

**Table 2.** Statistics of AOD and ANG retrievals for AERONET/MAN mid-visible AOD < 0.10\*.

Adjustment (blue)	$1\sigma$ (%)	$2\sigma$ (%)	68th % absolute error	RMSE	MAE	Med bias	#
SA	21	50	0.053	0.059	0.039	0.039	593
SA + 0.5 FNC	28	57	0.047	0.049	0.034	0.033	524
RA	52	81	0.029	0.036	0.019	0.016	593
RA + 0.5 FNC	62	88	0.023	0.028	0.016	0.011	524
RA + ghost	63	88	0.023	0.029	0.015	0.008	593
RA + ghost + 0.5 FNC	70	93	0.019	0.023	0.013	0.003	524
Adjustment (green)	$1\sigma$	$2\sigma$	68th % absolute error	RMSE	MAE	Med bias	#
SA	32	66	0.039	0.046	0.028	0.028	593
SA + 0.5 FNC	40	73	0.034	0.037	0.024	0.023	524
RA	55	83	0.026	0.033	0.018	0.015	593
RA + 0.5 FNC	62	89	0.022	0.026	0.014	0.011	524
RA + ghost	67	90	0.020	0.027	0.013	0.007	593
RA + ghost + 0.5 FNC	72	94	0.017	0.021	0.011	0.003	524
Adjustment (red)	$1\sigma$	$2\sigma$	68th % absolute error	RMSE	MAE	Med bias	#
SA	43	73	0.031	0.038	0.021	0.021	593
SA + 0.5 FNC	51	81	0.026	0.029	0.018	0.016	524
RA	55	83	0.025	0.032	0.017	0.015	593
RA + 0.5 FNC	63	90	0.021	0.025	0.014	0.010	524
RA + ghost	67	91	0.019	0.025	0.012	0.006	593
RA + ghost + 0.5 FNC	73	95	0.017	0.020	0.010	0.003	524
Adjustment (NIR)	$1\sigma$	$2\sigma$	68th % absolute error	RMSE	MAE	Med bias	#
SA	53	82	0.024	0.030	0.016	0.013	593
SA + 0.5 FNC	60	88	0.021	0.023	0.014	0.008	524
RA	56	83	0.023	0.030	0.016	0.013	593
RA + 0.5 FNC	62	88	0.020	0.024	0.013	0.008	524
RA + ghost	68	92	0.018	0.023	0.011	0.004	593
RA + ghost + 0.5 FNC	72	95	0.016	0.019	0.010	0.002	524
Adjustment (ANG)	$1\sigma$	$2\sigma$	68th % absolute error	RMSE	MAE	Med bias	#
SA	52	86	0.500	0.551	0.347	0.300	593
SA + 0.5 FNC	50	84	0.519	0.554	0.371	0.335	524
RA	73	93	0.340	0.457	0.220	-0.042	593
RA + 0.5 FNC	72	94	0.357	0.432	0.238	-0.052	524
RA + ghost	75	95	0.321	0.434	0.205	0.012	593
RA + ghost + 0.5 FNC	74	95	0.333	0.406	0.218	0.013	524

\* Columns 2 and 3 give the percent of validation cases within the confidence envelopes indicated. Column 4 lists the 68th percentile absolute errors (Eqs. 5 and 6 for AOD and ANG, respectively), Column 5 gives the RMSE, which is the root-mean-square error, MAE is the median absolute error, Med bias is the median bias, and # is the number of validation cases included. The first four data blocks give the spectral AOD statistics, and the fifth data block presents the ANG statistics.

into 50 bins containing equal numbers of points and determined the 68th percentile absolute errors corresponding to each AOD bin. Then a regression line was fit to the 68th percentile errors, and slope and intercept values were derived. The resulting AOD uncertainty envelope for the validation data set used here is

$$\text{AOD}_{\text{unc}} = \pm (0.10 \cdot \text{AOD}_{\text{spectral}} + 0.013), \quad (6)$$

where  $\text{AOD}_{\text{spectral}}$  is the AOD reported at any of the four wavelengths. The coefficients of this envelope do not vary substantially with wavelength. Also, we find that represent-

ing the ANG uncertainty as

$$\text{ANG}_{\text{unc}} = \pm (e^{-25 \cdot \text{AOD}_{\text{Green}}} + 0.15) \quad (7)$$

results in about 68 % of the ANG data falling within this uncertainty metric over the entire range of AOD. Note that this function represents the exponentially increasing MISR sensitivity to particle microphysical properties with increasing AOD (Kahn and Gaitley, 2015).

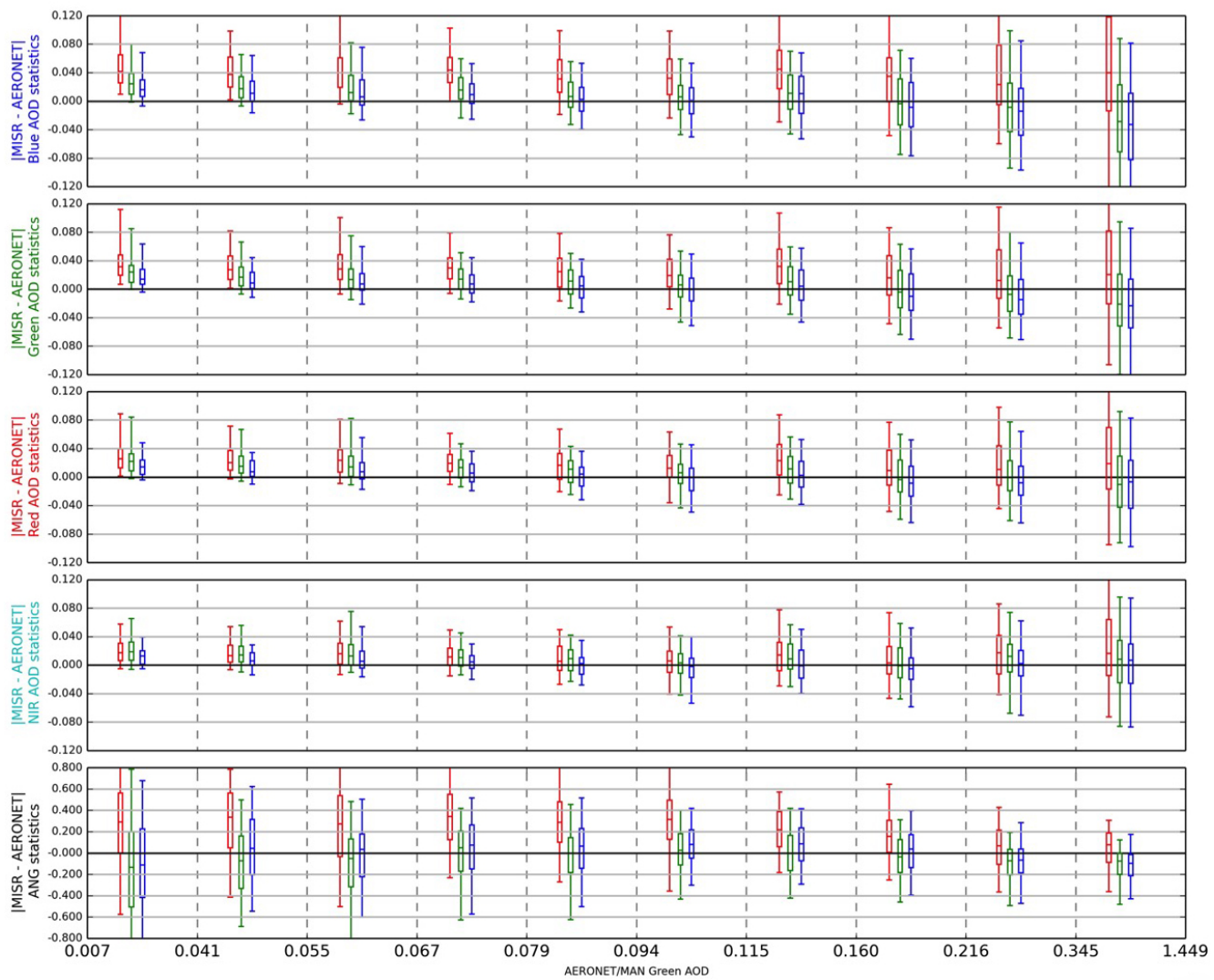


**Figure 9.**  $|\text{MISR} - \text{AERONET}|$  spectral AOD and ANG statistics conditioned on AERONET mid-visible AOD. For the vertical whiskers and points: red represents the SA, green represents the baseline RA, and blue represents the RA with stray light corrections applied. The box represents the 25th and 75th percentile errors, the dot represents the median error, and the whiskers indicate the 5th and 95th percentile errors. Each row of plots presents results for one of the four MISR spectral bands (blue, green, red, and NIR); the fifth row gives the corresponding results for ANG, assessed between 440 and 867 nm wavelength. Vertical dashed lines separate AOD bins, which are defined based on the AERONET or MAN mid-visible AOD. The upper limit of each mid-visible AOD bin is shown at the bottom of each plot.

#### 4.2 Validation against coincident AERONET and MAN data

Table 2 shows the statistics of ANG and AOD for low-AOD cases:  $\text{AERONET/MAN}_{\text{mid-vis}} \text{AOD} < 0.10$ . Compared to both the SA and the RA without the stray light corrections implemented, the upgraded RA shows substantial improvement, both with and without enhanced cloud screening, for every AOD statistic considered. With enhanced cloud screening and for  $\text{AOD} < 0.10$ , the upgraded RA reports a median mid-visible AOD bias of only 0.005 compared to 0.023 for the SA and 0.011 for the baseline RA. RMSE for the upgraded RA decreases by 14–25 % compared to the baseline

algorithm and by 22–51 % compared to the SA. Median absolute error (MAE) for the upgraded RA decreases by 12–29 % compared to the baseline algorithm and by 29–59 % compared to the SA.

Figure 9 shows the AOD and ANG results of including the stray light correction (blue whiskers) compared to the baseline RA (green whiskers) and the SA (red whiskers), as a function of mid-visible AERONET AOD, when enhanced cloud screening is not applied. Note that the stray light corrections improve the results substantially for the lowest AOD bins but have a smaller relative impact at higher AOD, as might be expected due to generally lower scene contrasts at

**Table 3.** Statistics of AOD and ANG retrievals for all AOD\*.

Adjustment (blue)	$1\sigma$ (%)	$2\sigma$ (%)	68th % absolute error	RMSE	MAE	Med bias	#
SA	31	60	0.061	0.073	0.042	0.038	1118
SA + 0.5 FNC	36	65	0.054	0.065	0.036	0.032	977
RA	56	84	0.037	0.047	0.024	0.010	1118
RA + 0.5 FNC	62	88	0.034	0.044	0.021	0.005	977
RA + ghost	62	89	0.032	0.043	0.021	0.002	1118
RA + ghost + 0.5 FNC	65	91	0.030	0.042	0.019	-0.002	977
Adjustment (green)	$1\sigma$	$2\sigma$	68th % absolute error	RMSE	MAE	Med bias	#
SA	42	72	0.044	0.056	0.030	0.026	1118
SA + 0.5 FNC	48	77	0.038	0.048	0.025	0.020	977
RA	60	86	0.031	0.041	0.021	0.010	1118
RA + 0.5 FNC	65	91	0.027	0.037	0.018	0.006	977
RA + ghost	67	91	0.027	0.037	0.018	0.002	1118
RA + ghost + 0.5 FNC	69	93	0.026	0.034	0.016	-0.001	977
Adjustment (red)	$1\sigma$	$2\sigma$	68th % absolute error	RMSE	MAE	Med bias	#
SA	50	78	0.037	0.047	0.023	0.019	1118
SA + 0.5 FNC	58	84	0.030	0.039	0.020	0.012	977
RA	60	87	0.028	0.037	0.019	0.010	1118
RA + 0.5 FNC	66	91	0.025	0.032	0.016	0.006	977
RA + ghost	68	91	0.024	0.033	0.017	0.003	1118
RA + ghost + 0.5 FNC	72	94	0.023	0.030	0.015	0.000	977
Adjustment (NIR)	$1\sigma$	$2\sigma$	68th % absolute error	RMSE	MAE	Med bias	#
SA	56	84	0.029	0.040	0.019	0.013	1118
SA + 0.5 FNC	63	90	0.025	0.033	0.016	0.007	977
RA	60	86	0.026	0.035	0.018	0.011	1118
RA + 0.5 FNC	66	90	0.024	0.029	0.016	0.005	977
RA + ghost	68	91	0.022	0.031	0.015	0.004	1118
RA + ghost + 0.5 FNC	72	94	0.021	0.027	0.014	0.000	977
Adjustment (ANG)	$1\sigma$	$2\sigma$	68th % absolute error	RMSE	MAE	Med bias	#
SA	47	80	0.398	0.455	0.280	0.216	1118
SA + 0.5 FNC	46	79	0.425	0.463	0.296	0.236	977
RA	66	89	0.275	0.373	0.173	-0.042	1118
RA + 0.5 FNC	66	89	0.282	0.360	0.181	-0.038	977
RA + ghost	69	91	0.247	0.354	0.159	-0.027	1118
RA + ghost + 0.5 FNC	68	91	0.262	0.339	0.167	-0.022	977

\* Columns 2 and 3 give the percent of validation cases within the confidence envelopes indicated. Column 4 lists the 68th percentile absolute errors (Eqs. 5 and 6 for AOD and ANG, respectively). Column 5 gives the RMSE, which is the root-mean-square error, MAE is the median absolute error, Med bias is the median bias, and # is the number of validation cases included. The first four data blocks give the spectral AOD statistics, and the fifth data block presents the ANG statistics.

higher atmospheric opacity. Although the RA performs better statistically at high AOD compared to the SA, it is important to point out that the RA is also biased low in the blue and green bands at high AOD. This is likely due to a combination of (a) lack of quantitative sensitivity to single-scattering albedo, (b) a sparse mixture grid in the algorithm climatology (lacking many absorbing mixture options), and (c) underlying calibration issues that would tend to show up at higher AOD (Kahn et al., 2010). The validation test statistics for 1118 validation cases are given in Table 3, aggregated over all AOD.

For all validation data with no enhanced cloud screening, the fraction of AOD data meeting our  $1\sigma$  error envelope increases by about 0.06–0.08 for all wavelengths compared to the baseline RA and by 0.12–0.31 compared to the SA. The median spectral bias decreases from 0.01 for the baseline RA and 0.01–0.04 for the SA to <0.005, and RMSE decreases by 2–11 % compared to the baseline RA and 22–37 % compared to the SA. Quantitatively, ANG does not change significantly compared to the baseline RA.

Figure 10 shows the AOD and ANG results similar to Fig. 9 but with the addition of enhanced cloud screening – a

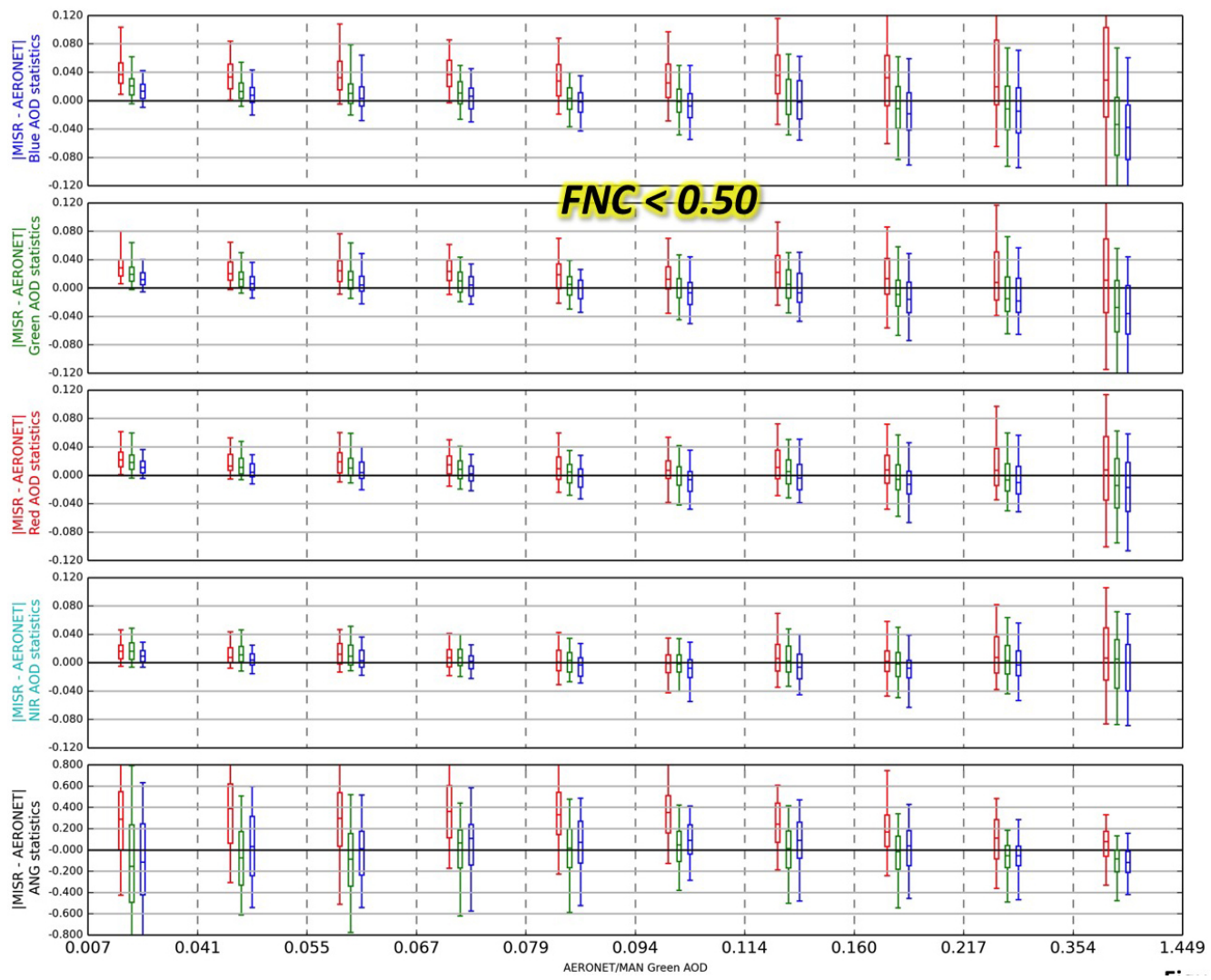


**Figure 10.**  $|\text{MISR} - \text{AERONET}|$  spectral AOD and ANG statistics conditioned on AERONET mid-visible AOD with enhanced cloud screening. Same as Fig. 9, except the fraction not clear (FNC) for the retrieval region must be  $< 0.5$ .

maximum FNC of 0.50, which removes 13 % of all  $3 \times 3$  regions compared to the validation data set with no additional cloud clearing applied. As Fig. 10 demonstrates, the AOD statistics improve for virtually every wavelength at low AOD with this modification and do not change much at higher AOD. Interestingly, unlike AOD, ANG does not change significantly with the ghosting corrections implemented. Table 3 shows that for all data with the enhanced cloud screening, the bias in AOD is now  $\leq 0.001$  for all wavelengths, and the bias in ANG aggregated over all AOD is also very small ( $< 0.02$ ). Statistically, the SA, the baseline RA, and the RA with the stray light corrections all improve with additional cloud screening. However, the improvement is much greater for the baseline RA and especially for the SA. This is primarily because the scenes containing the same objects that cause the most stray light, mainly bright clouds and sea ice

over dark water, tend to be removed as the maximum allowed FNC is reduced.

## 5 Conclusions

In Limbacher and Kahn (2014), we showed that a small positive bias remained in the RA at low AOD over ocean ( $\sim 0.01$  for the green at  $\text{AOD} < 0.10$ ), even with all the adjustments that were implemented in that study. We identify here the following types of stray light as contributing to, and possibly accounting fully for, the observed bias in TOA reflectance in high-contrast scenes that produces the AOD overestimation: primary ghosting convolved with background reflectance modulation, a smaller secondary ghosting term that acts on scene halves, blurring of contrast features, and possibly a uniform veiling-light term that is too small

to model explicitly with our empirical image analysis approach. We developed relationships to represent the primary ghosting, secondary ghosting, and blurring phenomena empirically and optimized the corresponding parameters for the MISR nadir camera using coincident MODIS imagery. The uniform veiling light is also at least partially taken into account by these other terms.

MODIS does not provide corresponding data for independently testing the other eight MISR cameras, so we applied the nadir corrections to the other channels under the assumption that the effects are dominated by similarities in the optics geometry of the different cameras; we then tested the results by comparing sun photometer validation data against AOD and ANG retrieved by the MISR RA under this assumption. Analysis of off-nadir camera performance is the subject of continuing work. Compared to the RA without the stray light corrections and to the SA, the corrections substantially improve spectral AOD agreement with the 1118 MAN/AERONET coincidences used for this study. For MAN/AERONET  $\text{AOD}_{558 \text{ nm}} < 0.10$ , 558 nm 68th percentile AOD errors decrease by 18 % compared to the RA and 47 % compared to the SA when we impose a maximum FNC of 0.50 as additional cloud masking. With all these corrections implemented, for  $\text{AOD}_{558 \text{ nm}} < 0.10$ , 68th percentile AOD errors for the mid-visible fall under 0.02.

The results presented here demonstrate that with our Limbacher and Kahn (2014) algorithm upgrades, a maximum FNC of 0.50, and stray light corrections, in addition to the reduction in random error, the  $\text{AOD}_{558 \text{ nm}}$  bias at low optical depth over ocean is reduced to 0.005. Furthermore, these corrections bring all MISR nadir band reflectances into much better agreement with MODIS. Ideally, the stray light corrections should be implemented in the MISR Level 1 processing to avoid the image-rotation complications discussed in Sect. 2.4 as well as the image trimming effects that are noticeable near the poles. Further analysis and possible refinement of the MISR absolute, channel-to-channel, and pixel-to-pixel calibration, and their variation over the MISR mission, are part of continuing work (Limbacher and Kahn, 2015, C. Bruegge, personal communication, 2015).

**Acknowledgements.** We thank our colleagues on the Jet Propulsion Laboratory's MISR instrument team and at the NASA Langley Research Center's Atmospheric Sciences Data Center for their roles in producing the MISR standard data sets, as well as our colleagues on the MODIS team, Brent Holben and the AERONET team, and Alexander Smirnov and the MAN team for the invaluable data sets they produce. We also thank Sergey Korkin, and Andrew Sayer for helpful discussions, Alexei Lyapustin for providing his MODIS radiometric correction code, Maksym Petrenko for identifying the MISR/MAN coincidences, and Carol Bruegge, James Butler, Veljko Jovanovic, and Michael Garay for comments on an early version of the manuscript. This research is supported in part by NASA's Climate and Radiation Research and Analysis Program under H. Maring, NASA's Atmospheric Composition Program

under R. Eckman, and the NASA Earth Observing System MISR instrument project.

Edited by: A. Sayer

## References

- Atlas, R., Hoffman, R. N., Ardizzone, J., Leidner, S. M., Jusem, J. C., Smith, D. K., and Gombos, D.: A cross-calibrated, multiplatform ocean surface wind velocity product for meteorological and oceanographic applications, *B. Am. Meteorol. Soc.*, 92, 157–174, doi:10.1175/2010BAMS2946.1, 2011.
- Barrot, G., Mangin, A., and Pinnock, S.: GlobColour Product User Guide, available at: <http://www.globcolour.info> (last access: 31 January 2014), 2010.
- Bruegge, C. J., Diner, D. J., Korechoff, R. P., and Lee, M.: MISR Level 1 Radiance Scaling and Conditioning Algorithm Theoretical Basis, Jet Propulsion Laboratory JPL D-11507, Rev E, available at: <http://eospso.gsfc.nasa.gov/sites/default/files/atbd/atbd-misr-02.pdf> (last access: 11 July 2014), 1999.
- Bruegge, C. J., Abdou, W. A., Diner, D. J., Gaitley, B. J., Helminger, M. C., Kahn, R. A., and Martonchik, J. V.: Validating the MISR radiometric scale for the ocean aerosol science communities, in: Post-Launch Calibration of Satellite Sensors, edited by: Morain, S. A. and Budge, A. M., A. A. Balkema Publishers, Leiden, The Netherlands, 103–115, 2004.
- Bruegge, C. J., Diner, D. J., Kahn, R. A., Chrien, N., Helminger, M. C., Gaitley, B. J., and Abdou, W. A.: The MISR radiometric calibration process, *Remote Sens. Environ.*, 107, 2–11, doi:10.1016/j.rse.2006.07.024, 2007.
- Bruegge, C. J., Diner, D. J., Gray, E., Jovanovic, V., Gray, E., Di Girolamo, L., and Zhao, G.: Radiometric stability of the Multi-angle Imaging SpectroRadiometer (MISR) following 15 years on-orbit, *Proc. SPIE 9218, Earth Observing Systems XIX*, 92180N, doi:10.1117/12.2062319, 2014.
- Chrien, N. L., Bruegge, C. J., and Gaitley, B. J.: AirMISR laboratory calibration and in-flight performance results, *Remote Sens. Environ.*, 77, 328–337, 2001.
- Diner, D. J., Kahn, R. A., Bruegge, C. J., Martonchik, J. V., Abdou, W. A., Gaitley, B. J., Helminger, M. C., Kalashnikova, O. V., and Li, W.-H.: Refinements to MISR's radiometric calibration and implications for establishing a climate-quality aerosol observing system, *SPIE Proc.*, 5652, 57–65, 2004.
- Eck, T. F., Holben, B. N., Reid, J. S., Dubovik, O., Smirnov, A., O'Neill, N. T., Slutsker, I., and Kinne, S.: Wavelength dependence of the optical depth of biomass burning, urban, and desert dust aerosols, *J. Geophys. Res.*, 104, 31333–31349, doi:10.1029/1999JD900923, 1999.
- Holben, B. N., Eck, T. F., Slutsker, I., Tanre, D., Buis, J. P., Setzer, A., Vermote, E., Reagan, J. A., Kaufman, Y. J., Nakajima, T., Lavenu, F., Jankowiak, I., and Smirnov, A.: AERONET – a federated instrument network and data archive for aerosol characterization, *Remote Sens. Environ.*, 66, 1–16, 1998.
- Jovanovic, V. M., Lewicki, S. A., Smyth, M. M., Zong, J., and Korechoff, R. P.: MISR Level 1 Georectification and Registration Algorithm Theoretical Basis, Jet Propulsion Laboratory JPL D-11532, Rev D, available at: <http://eospso.gsfc.nasa.gov/sites/>

- default/files/atbd/atbd-misr-03.pdf (last access: 11 July 2014), 1999.
- Jovanovic, V. M., Bull, M. A., Smyth, M. M., and Zong, J.: MISR In-flight camera geometric model calibration and georectification performance, *IEEE T. Geosci. Remote*, 40, 1512–1519, 2002.
- Kahn, R. A. and Gaitley, B. J.: An Analysis of Aerosol Type As Retrieved by MISR, *J. Geophys. Res. Atmos.*, 120, 4248–4281, doi:10.1002/2015JD023322, 2015.
- Kahn, R. A. and Limbacher, J.: Eyjafjallajökull volcano plume particle-type characterization from space-based multi-angle imaging, *Atmos. Chem. Phys.*, 12, 9459–9477, doi:10.5194/acp-12-9459-2012, 2012.
- Kahn, R. A., Banerjee, P., and McDonald, D.: The sensitivity of multiangle imaging to natural mixtures of aerosols over ocean, *J. Geophys. Res.*, 106, 18219–18238, 2001.
- Kahn, R., Li, W.-H., Martonchik, J., Bruegge, C., Diner, D., Gaitley, B., Abdou, W., Dubovik, O., Holben, B., Smirnov, S., Jin, Z., and Clark, D.: MISR low-light-level calibration, and implications for aerosol retrieval over dark water, *J. Atmos. Sci.*, 62, 1032–1062, 2005.
- Kahn, R. A., Gaitley, B. J., Garay, M. J., Diner, D. J., Eck, T., Smirnov, A., and Holben, B. N.: Multiangle imaging spectroradiometer global aerosol product assessment by comparison with the Aerosol Robotic Network, *J. Geophys. Res.*, 115, D23209, doi:10.1029/2010JD014601, 2010.
- Lallart, P., Kahn, R. A., and Tanré, D.: POLDER2/ADEOSII, MISR, and MODIS/Terra reflectance comparisons, *J. Geophys. Res.*, 113, D14S02, doi:10.1029/2007JD009656, 2008.
- Levy, R. C., Mattoo, S., Munchak, L. A., Remer, L. A., Sayer, A. M., Patadia, F., and Hsu, N. C.: The Collection 6 MODIS aerosol products over land and ocean, *Atmos. Meas. Tech.*, 6, 2989–3034, doi:10.5194/amt-6-2989-2013, 2013.
- Limbacher, J. A. and Kahn, R. A.: MISR research-aerosol-algorithm refinements for dark water retrievals, *Atmos. Meas. Tech.*, 7, 3989–4007, doi:10.5194/amt-7-3989-2014, 2014.
- Limbacher, J. A. and Kahn, R. A.: Empirical Corrections for MISR Calibration Temporal Trends, Point-Spread Function, Flat-Fielding, and Ghosting, *Atmosph. Meas. Tech.*, in preparation, 2015.
- Lyapustin, A., Wang, Y., Kahn, R., Xiong, J., Ignatov, A., Wolfe, R., Wu, A., Holben, B., and Bruegge, C.: Analysis of MODIS-MISR calibration differences using surface albedo around AERONET sites and cloud reflectance, *Remote Sens. Environ.*, 107, 12–21, doi:10.1016/j.rse.2006.09.028, 2007.
- Lyapustin, A., Wang, Y., Xiong, X., Meister, G., Platnick, S., Levy, R., Franz, B., Korkin, S., Hilker, T., Tucker, J., Hall, F., Sellers, P., Wu, A., and Angal, A.: Scientific impact of MODIS C5 calibration degradation and C6+ improvements, *Atmos. Meas. Tech.*, 7, 4353–4365, doi:10.5194/amt-7-4353-2014, 2014.
- Smirnov, A., Holben, B. N., Slutsker, I., Giles, D. M., McClain, C. R., Eck, T. F., Sakerin, S. M., Macke, A., Croot, P., Zibordi, G., Quinn, P. K., Sciare, J., Kinne, S., Harvey, M., Smyth, T. J., Piketh, S., Zielinski, T., Proshutinsky, A., Goes, J. I., Nelson, N. B., Larouche, P., Radionov, V. F., Goloub, P., Krishna Moorthy, K., Matarrese, R., Robertson, E. J., and Jourdin, F.: Maritime Aerosol Network as a component of Aerosol Robotic Network, *J. Geophys. Res.*, 114, D06204, doi:10.1029/2008JD011257, 2009.
- Sun, J., Angal, A., Xiong, X.-J., Chen, H., Geng, X., Wu, A., Choi, T.-J., and Chu, M.: MODIS reflective solar bands calibration improvements in collection 6, *Proc. SPIE* 8510, 85100J-1, doi:10.1117/12.930021, 2012.
- Xiong, X.-J. and Barnes, W. L.: An overview of MODIS radiometric calibration and characterization, *Adv. Atmos. Sci.*, 23, 69–79, 2006.